Journal of Hazardous Materials 451 (2023) 131075

Contents lists available at ScienceDirect

Journal of Hazardous Materials

journal homepage: www.elsevier.com/locate/jhazmat

Research Paper

A coupled electrochemical process for schwertmannite recovery from acid mine drainage: Important roles of anodic reactive oxygen species and cathodic alkaline

Ziyuan Huang [a], Huanxin Ma [a], Chengshuai Liu [b], Fangyuan Meng [b], Jyh-Fu Lee [c], Yu-Jung Lin [c], Xiaoyun Yi [a], Zhi Dang [a], Chunhua Feng [a,*]

[a] The Key Lab of Pollution Control and Ecosystem Restoration in Industry Clusters, Ministry of Education, School of Environment and Energy, South China University of Technology, Guangzhou 510006, PR China
[b] State Key Laboratory of Environmental Geochemistry, Institute of Geochemistry, Chinese Academy of Sciences, Guiyang 550081, PR China
[c] National Synchrotron Radiation Research Center, Hsinchu 30076, Taiwan, ROC

HIGHLIGHTS

- Schwertmannite is synthesized from AMD using a coupled electrochemical system.
- The system involves anodic Fe(II) oxidation and cathodic alkaline production.
- High currents result in schwertmannite high in SSA and amounts of –OH groups.
- •OH plays a dominant role in accelerating Fe(II) oxidation at high currents.
- Schwertmannite recovered from real AMD is a powerful sorbent for arsenic species.

GRAPHICAL ABSTRACT

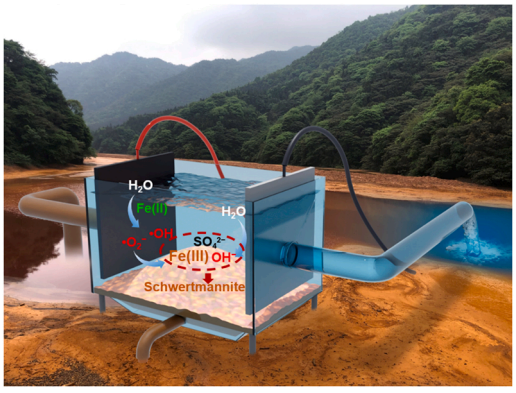

ARTICLE INFO

Editor: Shikha Garg

Keywords:
Acid mine drainage
Schwertmannite synthesis
Reactive oxygen species
Fe(II)-activated oxygen reduction
Adsorption of arsenic species

ABSTRACT

The increasing need for sustainable acid mine drainage (AMD) treatment has spurred much attention to strategic development of resource recovery. Along this line, we envisage that a coupled electrochemical system involving anodic Fe(II) oxidation and cathodic alkaline production will facilitate in situ synthesis of schwertmannite from AMD. Multiple physicochemical studies showed the successful formation of electrochemistry-induced schwertmannite, with its surface structure and chemical composition closely related to the applied current. A low current (e.g., 50 mA) led to the formation of schwertmannite having a small specific surface area (SSA) of 122.8 $m^2\ g^{-1}$ and containing small amounts of –OH groups (formula $Fe_8O_8(OH)_{4.49}(SO_4)_{1.76}$), whereas a large current (e.g., 200 mA) led to schwertmannite high in SSA (169.5 $m^2\ g^{-1}$) and amounts of –OH groups (formula $Fe_8O_8(OH)_{5.16}(SO_4)_{1.42}$). Mechanistic studies revealed that the reactive oxygen species (ROS)-mediated pathway, rather than the direct oxidation pathway, plays a dominant role in accelerating Fe(II) oxidation, especially at

* Corresponding author.
E-mail address: chfeng@scut.edu.cn (C. Feng).

https://doi.org/10.1016/j.jhazmat.2023.131075
Received 24 December 2022; Received in revised form 11 February 2023; Accepted 22 February 2023
Available online 2 March 2023

high currents. The abundance of •OH in the bulk solution, along with the cathodic production of OH^-, were the key to obtaining schwertmannite with desirable properties. It was also found to function as a powerful sorbent in removal of arsenic species from the aqueous phase.

1. Introduction

Acid mine drainage (AMD), which results from chemical/biological oxidation of sulfide minerals (e.g., pyrite) upon exposure to oxygen, water, sunlight, and bacteria [7,13,41], represents a worldwide environmental concern. It contains elevated concentrations of protons (H^+), ferrous/ferric iron (Fe(II)/Fe(III)), sulfate (SO_4^{2-}), and a variety of other metals depending on the mineral sources, and severely damages downstream water quality and soil ecology if not treated. The most widely used method to remediate AMD is lime neutralization, which precipitates Fe and heavy metals by alkali addition [53,57]. Despite its simplicity and ease of operation, this method has unavoidable shortcomings: production of large-quantity sludge needing further disposal and loss in reaction efficiency due to precipitation coating on lime particles, both of which ultimately add to operational costs. The increasing requirement for sustainable AMD treatment has stimulated research to develop new methods of recovery of valuable solid products. The recovery of Fe and SO_4^{2-} from AMD by forming schwertmannite (an excellent and environmentally-friendly adsorption material for heavy metals) has recently attracted much attention because of its environmental and economic benefits [65]. The commonly-adopted approach to schwertmannite synthesis from AMD is via biological oxidation of Fe(II) by *Acidithiobacillus ferrooxidans*, which is cost-effective but time-consuming [29]. The addition of H_2O_2 to oxidize Fe(II) to obtain schwertmannite is a rapid process [45], but requires transport and storage of high-cost H_2O_2. Moreover, the H_2O_2-involved chemical process yields schwertmannite with a lower specific surface area (SSA) than via biological oxidation [6,39,45], a critical characteristic determining its adsorption capacity.

This study offers a promising method of electrochemical production of high-SSA schwertmannite in a short time. The principle lies in the coupling of anodic and cathodic reactions, during which Fe(II) oxidation (Eq. (1)) [10], surface •OH production (Eq. (2)) [48], and O_2 evolution (Eq. (3)) [48,54] reactions at the anode side and Fe(III) reduction (Eq. (4)) [33] and OH^- generation (Eq. (5)) [26] reactions at the cathode side can be paired to facilitate on-site production of high-value schwertmannite (Eq. (6)) [32]. It is hypothesized that the localized high pH in the vicinity is not only conducive to the formation of schwertmannite, but also affords the alkaline environment that induces Fe(II) oxidation by dissolved O_2 through a series of one-electron transfer reactions (Eqs. (7)–(10)) [20,25]. These reactions would allow the continuous formation of diverse reactive oxygen species (ROS, such as $\bullet O_2^-$, H_2O_2, and •OH), which play significant further roles in mediating Fe(II) oxidation to schwertmannite [60]. It can thus be inferred that both direct anodic oxidation and ROS-involved oxidation contribute to Fe(II) conversion to solid-phase Fe(III), but the extent of the contribution of each remains unknown. Moreover, it is of interest to determine whether the morphology, SSA, and chemical composition of schwertmannite are closely linked to the oxidation pathway.

$$Fe(II) \rightarrow Fe(III) + e^- \quad (1)$$

$$2H_2O \rightarrow \equiv HO\bullet + H_2O + H^+ + e^- \quad (2)$$

$$2H_2O \rightarrow 4H^+ + O_2 + 4e^- \quad (3)$$

$$Fe(III) + e^- \rightarrow Fe(II) \quad (4)$$

$$2H_2O + 2e^- \rightarrow 2OH^- + H_2 \quad (5)$$

$$8Fe(III) + xSO_4^{2-} + (16 - 2x)OH^- \rightarrow Fe_8O_8(OH)_{8-2x}(SO_4)_x + 8H^+ \quad (6)$$

$$Fe(II) + O_2 \rightarrow Fe(III) + \bullet O_2^- \quad (7)$$

$$Fe(II) + \bullet O_2^- + 2H^+ \rightarrow Fe(III) + H_2O_2 \quad (8)$$

$$Fe(II) + H_2O_2 \rightarrow Fe(III) + \bullet OH + OH^- \quad (9)$$

$$Fe(II) + \bullet OH \rightarrow Fe(III) + OH^- \quad (10)$$

The primary objectives of this study are therefore i) to demonstrate the concept of a coupled anodic-cathodic process for schwertmannite recovery from AMD with high efficacy and ii) to elucidate the role of in-situ generated ROS on controlling schwertmannite with desirable characteristics. Because the applied current density is a key variable influencing the extent and rate of direct anodic Fe(II) oxidation, anodic oxygen evolution, and cathodic OH^- generation, which together determine the type and level of ROS, attempts were made to establish the relationship between the current density and schwertmannite properties. The disclosure of such dependence was obtained with the help of a series of physicochemical characterizations. To further confirm these findings, tests with real AMD samples were conducted and assessments of the resulting schwertmannite materials for As(III)/As(V) adsorption were performed.

2. Material and methods

2.1. Chemicals and electrode materials

Iron sulfate heptahydrate ($FeSO_4 \bullet 7H_2O$), anhydrous sodium sulfate ($NaSO_4$), sodium formate (NaCOOH), tertiary butanol (TBA), benzoic acid (BA), and 5,5-dimethyl-1-pyrroline N-oxide (DMPO) were purchased from Aladdin Industrial Corporation (Shanghai, China). The As(III) and As(V) stock solutions were prepared by dissolving dehydrated arsenic oxide (As_2O_3) and disodium hydrogen arsenate heptahydrate ($Na_2HAsO_4 \bullet 7H_2O$) in deionized (DI) water, respectively. All other reagents were of at least analytical grade and used without further purification. A mixed metal oxide (MMO) electrode (IrO_2–RuO_2/Ti; Changli Specialty Metals Ltd., Shanxi, China) and stainless-steel plate electrode (304 type, Zhong Run Hongfa Stainless Steel Co., Ltd., Shenzhen, China) were employed in electrochemical reactors (both electrodes have a size of 30 × 30 mm with a thickness of 1 mm). DI water was used throughout this study.

2.2. Batch experiments

The constant-current electrolysis experiments were performed in an undivided cylindrical glass electrolytic cell having an effective volume of 300 mL. An MMO electrode and a stainless-steel plate electrode were placed with a gap of 15 mm in the electrochemical reactor, which was powered by a DC power supply (GPD2303S, GWINSTEK, Suzhou, China). The simulated AMD was composed of 500 mg L^{-1} Fe(II) and 4 g L^{-1} SO_4^{2-}, and had an initial pH of 3.0. The real AMD sample was collected from Dabaoshan (Shaoguan, Guangdong province, China). The main water quality characteristics are shown in Table S1. To examine the effect of the current on the performance of Fe(II) oxidation, the current applied to the circuit was varied from 10 to 250 mA. For comparison, similar electrolysis tests were also conducted in divided cells, in which the anode and cathode chambers were separated by an anion-exchange membrane (AEM, AMX, Astom Co., Tokyo, Japan), a cation-exchange membrane (CEM, CMX, Astom Co., Tokyo, Japan), or a bipolar membrane (BPM, BP-1E, Astom Co., Tokyo, Japan). All the electrochemical experiments were carried out at a temperature of 25 ± 0.5 °C, and the electrolyte pH was not adjusted at any time during the

process. The liquid samples were taken with syringes at regular intervals and immediately filtered by a 0.22 μm membrane for further analysis. The solid samples were obtained from the suspension by successive vacuum extraction, freeze drying, and grinding, and were stored at 4 °C for further physicochemical characterization.

To determine the contribution of ROS to Fe(II) oxidation in AMD, probe and scavenging experiments were conducted in the same reactor. BA was used as a probe to quantify the steady-state concentration of •OH [27]. NaCOOH and TBA were used as scavengers to extinguish surface-bound •OH [9] and bulk •OH [60], respectively. The adsorption experiments were conducted at pH 3.0 in a 100 mL conical flask, which was oscillated on a horizontal vibrator at 180 rpm and 25 ± 0.5 °C. The solution contained 0.01 g schwertmannite and varying initial concentrations of As(III)/As(V) at 1, 10, 20, 30, 40, and 50 mg L^{-1}. All tests were repeated in triplicate. Average results are reported throughout the study.

2.3. Physicochemical characterizations

The crystalline structures of the solid products were characterized by X-ray diffractometer (XRD, Bruker D8 Advance diffractometer, Almelo, The Netherlands) with Cu Kα, λ = 0.15418 nm, with the XRD patterns collected at a step of 0.026 using a scanning rate of 2° min^{-1} from 10° to 70°. The functional groups were determined by Fourier-transform infrared spectroscopy (FTIR, Bruker VERTEX 70, Waltham, MA, USA). The morphology and particle size of the samples were examined through field emission scanning electron microscopy (SEM, Merlin, Zeiss Co., Berlin, Germany). Mössbauer spectra were collected at 13 K in transmission mode and a WSS-10 Mössbauer spectrometer (WissEL GmbH, Germany) equipped with a closed cycle cryostat (SHI-850, Janis Research Co., Wilmington, MA, USA). All spectra were calibrated against 7 μm α-Fe(0) foil and fitted using Mosswinn software. The SSA of the samples was measured using Micromeritics ASAP 2460 BET apparatus (Micromeritics ASAP 2460, USA). The Fe K-edge X-ray absorption spectra were obtained in transmission mode at beamline 17C at the National Synchrotron Radiation Research Center (NSRRC). The obtained XAFS data was processed in Athena (version 0.9.26) for background, pre-edge line, and post-edge line calibrations. The Fourier transformed fitting and liner combination fitting (LCF) were carried out using Artemis (version 0.9.26) [44].

2.4. Analysis and calculations

The concentrations of Fe(II) and total Fe (TFe) were detected at 510 nm using the 1,10-o-phenanthroline analytical method with a UV–vis spectrophotometer (UV-2550, Shimadzu, Kyoto, Japan). Bulk solution pH was monitored using a pH meter (Leici PHB-4, INESA Scientific Instrument, Shanghai, China). A pH electrode (Ø 3 mm, LabSen, Shanghai, China) was placed close to the cathode (~ 1.0 mm) to identify the dynamic change of localized pH in its vicinity. The concentration of BA was detected using a high-performance liquid chromatograph (HPLC, LC-20AT, Shimadzu, Kyoto, Japan). The EPR experiments were performed using a spectrometer (EMX-10/12, Bruker, Karlsruhe, Germany). Determination of total arsenic and As(III) species was carried out using hydride generation atomic fluorescence spectrophotometry with a detection limit of 0.1 μg L^{-1} (AFS-PF6, Purkinje General Instrument Corp., Beijing). Linear sweep voltammetry (LSV) measurement was conducted with an electrochemical workstation (CHI760e, Chenhua Instruments, Shanghai, China) under the three-electrode mode (MMO, Pt mesh, and saturated calomel electrode were used as the working, counter, and reference electrodes, respectively). The simulated AMD was used as the electrolyte with a scan rate of 10 mV s^{-1}.

The Coulombic efficiency (CE, %) of Fe(II) oxidation was defined as the ratio of the theoretical coulombs calculated from the specific amount of Fe(II) oxidized to Fe(III) to the coulombs actually applied to the electrode (Eq. (11)).

$$CE = \frac{n \times F \times (C_o - C_t) \times V}{1000 \times 56 \times 60 \times I \times t} \times 100 \quad (11)$$

Where n is the number of electrons required per mol of Fe(II) oxidized; F represents the Faraday constant (96,485.3 C mol^{-1}); C_0 and C_t refer to the concentrations (mg L^{-1}) of the Fe(II) at the reaction times of 0 and t (s), respectively; V is the volume of the reactor; I is the current (A); t is the electrolytic time (min);56 is the molar mass of Fe (g mol^{-1}), and 60 is a unit conversion factor (60 s min^{-1}). The specific energy consumption (SEC, kWh g^{-1} (Fe solid)) was calculated via Eq. (12):

$$SEC = \frac{U \times I \times t}{60 \times m} \quad (12)$$

where U is the applied voltage (V); I is the average current (A); t is the electrolytic time (min); and m refers to the quantity of Fe solid (g).

3. Results and discussion

3.1. Efficient Fe(II) and SO_4^{2-} removal and recovery by the coupled anodic-cathodic process

To verify the importance of anodic-cathodic coupling for Fe(II) removal, an undivided cell and two divided cells (with AEM or CEM as the separation membrane) were constructed, and the time courses of Fe (II) concentration in these electrochemical reactors were evaluated. As illustrated in Fig. 1a, negligible removal of Fe(II) was seen under the open-circuit condition, indicating that very little Fe(II) oxidation by dissolved O_2 occurs at pH 3.0. The slowness of the reaction between Fe (II) and O_2 in the acidic pH region has been testified in previous studies [23,52]. When the same current density (i.e., 200 mA) was applied for 180 min, the undivided system with the paired anodic-cathodic reactions enabled significantly greater Fe(II) removal from the aqueous phase (371.0 mg L^{-1} Fe(II)) than the divided system equipped with AEM and CEM (134.4 and 153.9 mg L^{-1} Fe(II) removal). This considerable difference is considered to be due to supplemental OH^- resulting from the cathodic water electrolysis reaction [26]. The increasing alkaline induced the hydrolysis of Fe(II) to form Fe species with higher reducibility (e.g. $Fe(OH)^+$, $Fe(OH)_2$, and $Fe(OH)_3^-$) [24,50]. These species can be more easily oxidized by dissolved O_2 even the bulk pH solution was maintained at a highly acidic value. Fig. S1a provides evidence that the bulk pH values in the undivided cell declined with a lower rate than those in the divided cells (AEM & CEM) due to continuous OH^- generation from the cathode and its diffusion into the solution. The localized alkaline pH favorable to solid Fe formation was indicated by the preferred coverage of Fe precipitates on the cathode surface (Fig. S2).

The current applied to the circuit determines both the anodic and cathodic reactions, being an important factor affecting Fe(II) removal and recovery. It is apparent from Fig. 1b that the rate of Fe(II) disappearance was highly dependent on the current intensity. Increasing the current from 50 to 200 mA drastically enhanced the Fe(II) oxidation efficiency from 36.3 % to 74.2 % after 180 min. A further increase to 250 mA did not distinctly augment the amount of removed Fe(II). This was attributed to sluggish mass transfer at a large current, a phenomenon frequently reported with respect to many anode electrocatalysts for oxygen evolution [8,35]. The disappearance of Fe(II) was found to obey the apparent first-order kinetic law, and the rate constant rose from 2.78×10^{-3} (50 mA) to 1.02×10^{-2} min^{-1} (200 mA). Taking into account the fairly narrow pH range (from 2.3 to 3.0) throughout the electrolysis test (Fig. S1b), it can be deduced that the valence of Fe in the solid phase was + 3 instead of + 2 (because $Fe(OH)_2$ does not precipitate in this pH range [49]), and that Fe(II) oxidation is a prerequisite for the precipitation. It is generally recognized that under acid conditions (e.g., pH at 2.5–4.5), the Fe(III) solid was most likely in the form of schwertmannite particularly in the presence of SO_4^{2-} [2,46,59]. Fig. 1c supports that a fraction of SO_4^{2-} was removed from the aqueous phase,

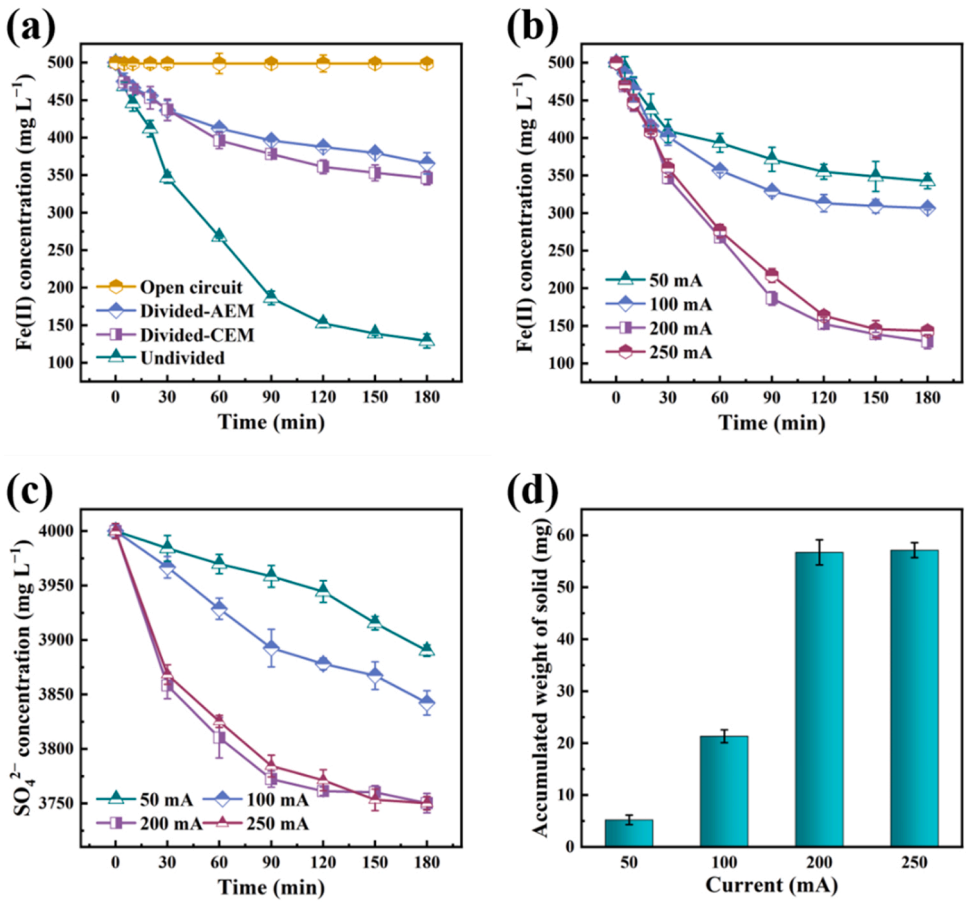

Fig. 1. (a) Time courses of Fe(II) concentration in different electrochemical systems at 200 mA. Effects of current on time courses of (b) Fe(II) concentration, and (c) SO_4^{2-} concentration, and (d) accumulated weight of the solid produced in the coupled anodic-cathodic reaction system. Experimental conditions: initial pH = 3.0, initial Fe(II) concentration = 500 mg L^{-1}, and initial SO_4^{2-} = 4000 mg L^{-1}.

with the larger quantities obtained at high currents. The accumulated weight of the solid was quantified and displayed in Fig. 1d. The higher current led to a larger yield, closely consistent with the amounts of Fe(II) and SO_4^{2-} eliminated from the solution. Overall, the data shown in Fig. 1 validate the conclusion that the coupled anodic-cathodic process is effective in phase transformation of Fe(II) and SO_4^{2-}, and that the rate is dependent on the current.

The CE and SEC provide information on the extent of electrons utilized for the desirable reactions. As shown in Fig. S3, the divided system with AEM or CEM exhibited remarkably decreased CE values and enhanced SEC values compared to the undivided system, again supporting the prominent role of cathodic alkaline in facilitating Fe(II) oxidation. When the current increased from 50 to 200 mA, it is anticipated that more electrons would participate in oxygen evolution reaction, resulting in the reduction in CE. However, the CE at 200 mA was 18.94 %, even slightly higher than 17.38 % at 50 mA; it thus can be deduced that the electrogenerated oxygen should be indirectly involved for Fe(II) conversion to Fe(III) solid (this point will be discussed in a later section). The current rose from 200 to 250 mA led to decreased CE, reflecting less amounts of electrons contributing to Fe(II) removal. Note that the measured CEs were relatively low, which can be further improved by promoting alkaline production via increasing the number of the cathodes for future studies. The increase in CE and the decrease in SEC was of high relevance for all the conditions. The coupled anodic-cathodic system at 200 mA appears to have the minimum SEC value of 0.017 kWh g^{-1}, equivalent to an estimated cost of 12.5 Chinese Yuan (CNY) per ton of Fe solids (taking into account the average electric price of 0.6 CNY kWh^{-1}). This was much lower than 76.5 CNY per ton Fe solids roughly calculated from the chemical method (based on the H_2O_2 price of 10.0 CNY kg^{-1}), manifesting the economic benefit of the electrochemical method.

3.2. *Comparisons of the physicochemical properties of electrosynthesized iron precipitates*

A series of physicochemical characterizations was conducted to elucidate the differences between the electrosynthesized iron minerals in surface morphology, chemical structure, and elemental composition. For comparisons, the chemically synthesized iron oxide (with the help of H_2O_2 oxidation) was subjected to the same characterizations. It is noticeable from Fig. 2 (inset pictures) that the exterior color changed from yellow to brown with increasing current, implying variations in surface structure and composition of different samples. The SEM images in Fig. 2 show that the as-obtained iron solids were composed of spheroidal particles with rough surfaces, differing from the hedgehog-like surface morphology obtained by biosynthesis [15]. The particle size from electrosynthesis was smaller than that obtained by chemical synthesis, and decreased with increasing current (especially from 50 to 100 mA). In the XRD patterns (Fig. 3a), all the solid samples exhibited the typical diffraction peaks of schwertmannite (JCPDS 47-1775). However, despite the appearance of one distinct peak, the intensities of other peaks were quite weak due to the metastable nature of schwertmannite. It is also difficult to distinguish the presence of other amorphous minerals (like ferrihydrite) from XRD patterns. Nevertheless, the Mössbauer spectra in Fig. 3b show six-line subspectra (sextets) in all the electrosynthesized samples as well as that produced by H_2O_2, which are characteristics of schwertmannite [22,40,51]. No other subspectra were discerned (Table S2), suggesting a high purity of schwertmannite.

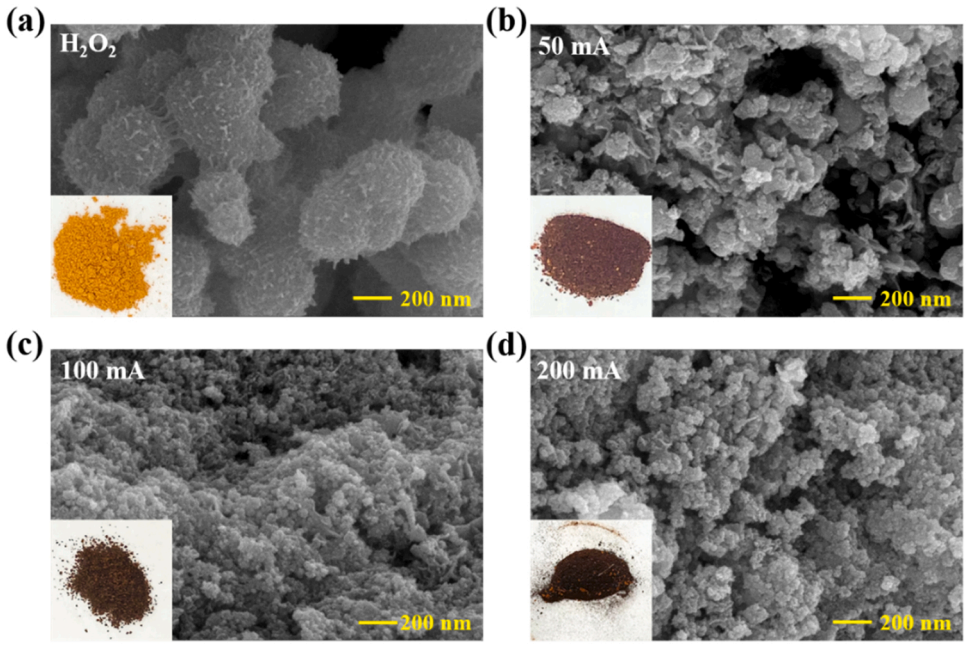

Fig. 2. SEM images of solid samples obtained under different conditions: (a) H_2O_2, (b) 50 mA, (c) 100 mA, and (d) 200 mA. The inset shows the sample photos.

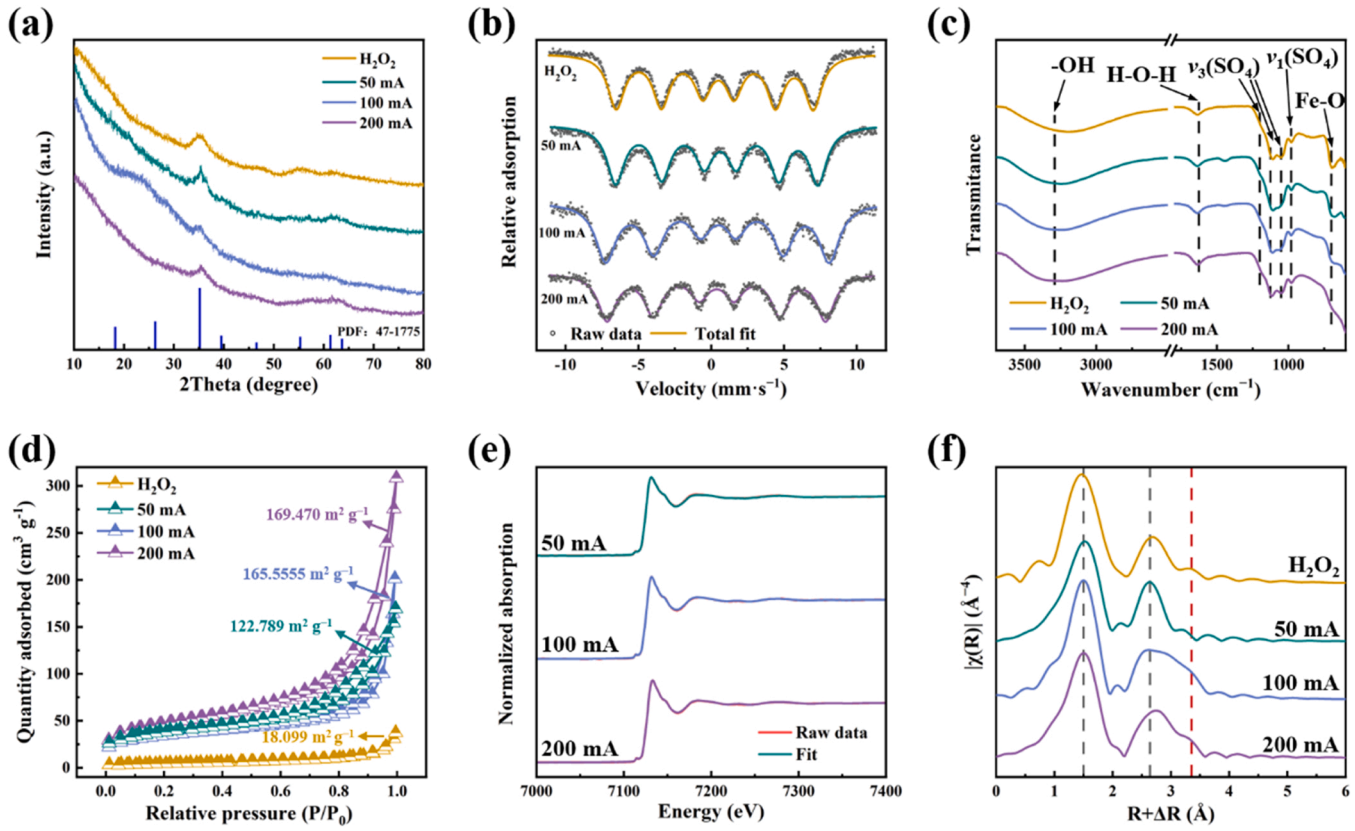

Fig. 3. (a) XRD patterns, (b) Mössbauer spectra, (c) FTIR, (d) N_2 adsorption-desorption isotherms, and (e) LCF of the measured EXAFS spectra of solid samples obtained under different conditions. (f) Magnitude (|χ(R)|) of Fourier transforms of K-edge EXAFS spectra.

Despite evidence for schwertmannite formation in all cases, its chemical structure may differ between samples. As depicted in the FTIR curves (Fig. 3c), the absorption bands at 980, 1050, 1125, and 1200 cm^{-1} are attributed to the S–O stretching vibration in SO_4^{2-} [56], and the absorption band at 700 cm^{-1} belong to the Fe–O stretching vibration [2,62]. One can see that the ~ 3291 and 1626 cm^{-1} peaks ascribed to O–H stretching vibration [3] have different intensities. Increased O–H band intensity is seen in the samples with elevated currents. This observation indicates that the electrosynthesized schwertmannite contained a greater amount of O–H groups than H_2O_2-produced schwertmannite, which was more manifest at a higher current. The fitting of O(1s) XPS signals (Fig. S4) with O1, O2, and O3 respectively

corresponding to S—O, Fe—OH, and Fe—O bonds also reveals that the proportion of Fe–OH in schwertmannite increased in the order of 200 mA > 100 mA > 50 mA > H_2O_2-produced samples. The SSA of schwertmannite was calculated by the N_2 adsorption-desorption isotherms (Fig. 3d), which was highly dependent on synthesis conditions. The electrochemistry-induced schwertmannite had an SSA of 18.19 m^2 g^{-1}, consistent with results in the literature [39,45], significantly higher than that produced by H_2O_2. By contrast, the SSAs of electrosynthesized schwertmannites were 122.8, 165.5, and 169.5 m^2 g^{-1}, with applied currents of 50, 100, and 200 mA, respectively. This trend accords well with the SEM observation, as smaller particles up to the nanometer scale were generated at higher currents. After determining the amounts of Fe and SO_4^{2-} in schwertmannite, the stoichiometric formulas were obtained (Table S3). Schwertmannite obtained from chemical and electrochemical synthesis at 50, 100, and 200 mA could be respectively expressed as $Fe_8O_8(OH)_{4.01}(SO_4)_{2.00}$, $Fe_8O_8(OH)_{4.49}(SO_4)_{1.76}$, $Fe_8O_8(OH)_{5.03}(SO_4)_{1.49}$, and $Fe_8O_8(OH)_{5.16}(SO_4)_{1.42}$, suggesting increasing –OH content with increasing applied current, which made the smaller particle size of schwertmannite (see Section 3.4 for details). The stoichiometry molar ratio of Fe/S in these formulas did not conform to the molar ratio of Fe(II) and SO_4^{2-} removed from the aqueous solution. This is due to the fact that the schwertmannite produced in solution can absorb SO_4^{2-} [5,55]. It is also observed that the increase in the current provoked an elevated molar ratio of Fe/S (Table S3), which should be responsible for the difference in the color of schwertmannite [66].

Structural differentiation at the atomic level was further explored by the EXAFS spectra and their fitting results (Table S4). The pure schwertmannite mineralogy was supported by the LCF of the measured EXAFS spectra obtained at different currents using H_2O_2-synthesized schwertmannite as the standard, which indicated a 100 % similarity (Fig. 3e). The local atomic environment around central Fe was illustrated by the Fe K-edge EXAFS spectroscopy (Fig. 3f). The peaks at 1.5 Å (R + ΔR) in |χ(R)| are ascribed to the nearest O shell, with a Fe–O distance of ~ 1.97 Å corresponding to the Fe—O bond length [11]. The peaks at ~ 2.60 Å and ~ 3.35 Å (R + ΔR) are assigned to the edge- and corner-sharing Fe shells at the Fe-Fe distances of ~ 3.01 Å and ~ 3.44 Å, respectively [11,67]. As the applied current increased, the two Fe–Fe peaks became more pronounced. The third coordination of Fe detected in such cases was considered to be the consequence of the compression of interplanar spacing. The results of XRD in Fig. 3a also evidenced a smaller interplanar spacing in schwertmannite generated from high currents, as indicated by the positive shift of the peak at 35.2°. The reduction in interplanar distance may result in more Fe atoms available in the schwertmannite crystal, which ultimately attracts more –OH groups being attached. These results collectively demonstrate that the current significantly altered the intrinsic chemical structure of schwertmannite, with higher contents of –OH species attained at increasing currents.

3.3. Identification of ROS and its role in enhancing Fe(II) oxidation at high currents

The enhancement of Fe(II) oxidation with increasing current is explained in terms of the reaction pathways, which generally include direct and indirect oxidation mediated by ROS. The dominance of one over the other is heavily dependent on the current applied onto the anode, which determines the occurrence of direct Fe(II) oxidation and/or anodic •OH electrogeneration (a prerequisite for anodic oxygen evolution). The LSV results (Fig. S5) show that there was a distinct anodic peak at 0.49 V (vs. SCE) attributed to Fe(II) oxidation, which happens significantly ahead of the oxygen evolution reaction at potentials larger than 1.20 V (vs. SCE). This suggests that Fe(II) is thermodynamically susceptible to direct oxidation at lower currents associated with lower potentials. However, for the currents at 10 and 25 mA, tiny amounts of Fe(II) were oxidized at pH 3 (Fig. S6), indicating sluggish kinetics even at the potentials of 0.52 and 1.14 V (vs. SCE), respectively. For the investigated currents of 50, 100, and 200 mA, the relevant potentials at the anode were recorded to be 1.56, 1.85, and 2.34 V (vs. SCE), respectively, substantially surpassing the potential of 1.20 V. This suggests that both anodic Fe(II) and water oxidation reactions can take place; the latter reaction presumably leads to the generation of surface-bound •OH and O_2 (Eqs. (2) and (3)). It is likely that both direct electron transfer and indirect mediation by surface-bound •OH can trigger the transformation of Fe(II), resulting in the formation of Fe(III) precipitate at pH 3 (K_{sp} of $Fe^{III}(OH)_3$ is 2.0×10^{-15}). Despite the retardation of the reaction between aqueous Fe(II) and O_2, the adsorbed Fe(II) on the Fe(III) solid is more susceptible to being oxidized by O_2, owing to the decreased redox potential of (≡Fe(III)/≡Fe(II)) [28], ultimately yielding the generation of $\bullet O_2^-$, H_2O_2, and •OH via the Haber-Weiss reaction (Eqs. (7)–(9)) [25,47]. These ROS, in turn, facilitate the oxidation of both aqueous and adsorbed Fe(II). It should be noted that no H_2O_2 was detected throughout the electrolysis process, when the electrolyte did not contain Fe(II). This indicates that the possible reduction of dissolved oxygen at the stainless state cathode did not contribute to H_2O_2 formation.

The presence of $\bullet O_2^-$ and •OH was confirmed by DMPO-probed EPR tests (Figs. 4a–c). For short-time treatment (i.e., 1 min) under all of the electrolysis conditions, the sextet signal was clearly visible, consistent with the literature concerning Fe(II) oxidation by dissolved oxygen to the generation of $\bullet O_2^-$ [30,42,64]. When p-benzoquinone (PBQ), a good scavenger of $\bullet O_2^-$, was added, the intensities of sextet peaks under all the conditions were attenuated (Fig. S7), confirming that the peaks are characteristic of DMPO-OOH adducts. It is interesting to observe that the 5 min operation resulted in the appearance of legible signals of DMPO-OH adducts in all cases and that the signals of DMPO-OOH adducts completely vanished at an applied current of 200 mA. Further extension of the reaction time to 10 min caused the disappearance of DMPO-OOH peaks for all currents investigated. The intensities of •OH-relevant peaks increased with increasing current, indicative of increasing •OH levels.

To provide more compelling evidence to support this view, BA, a probe that has been used effectively to determine the steady-state concentration of •OH [27,61], was used to quantify and compare •OH concentrations in the electrolysis system with different applied currents. To distinguish the contribution of interfacial electron transfer to the anodic conversion of BA, reference experiments were conducted in the absence of aqueous Fe(II) and benchmarked with those containing Fe(II). Fig. 4d shows that the first-order rate constants of k_{BA} in the absence of Fe(II) in relation to 50, 100, and 200 mA were 7.60×10^{-4}, 8.56×10^{-4}, and 9.74×10^{-4} min^{-1}, respectively. The involvement of Fe(II) significantly increased the rate constants at high currents (e.g., 1.45×10^{-3} min^{-1} for 100 mA and 1.89×10^{-3} min^{-1} for 200 mA), but only slightly increased the rate constant at 50 mA (e.g., 9.85×10^{-4} min^{-1}), as shown in Fig. 4e. These results suggest that the interfacial oxidation plays a predominant role in the case of 50 mA, and that the bulk oxidation mediated by •OH should be the main pathway with increasing currents. By subtracting the contribution of interfacial anodic oxidation, the steady-state concentrations of •OH were estimated to be 5.24×10^{-14}, 1.38×10^{-13}, and 2.13×10^{-13} M corresponding to 50, 100, and 200 mA, respectively (Fig. 4f), reinforcing the conclusion that increased current is conducive to the generation of •OH. It is particularly noted from Fig. S8 that a further increase in the current at 250 mA yielded 2.16×10^{-13} M •OH comparable to that (2.13×10^{-13} M) obtained at 200 mA. This result is closely linked to the insignificant improvement in the oxidation of Fe(II) oxidation because of the mass-transfer limitation at the increasing current [8,35].

Scavenging experiments were conducted to further investigate the main pathways involved in Fe(II) oxidation at different currents. Formate and TBA, which are capable of quenching surface-bound •OH and bulk •OH, respectively, were selected to determine the main contribution to Fe(II) oxidation. Considering that surface-bound •OH generated from water electrolysis is an essential precursor to the

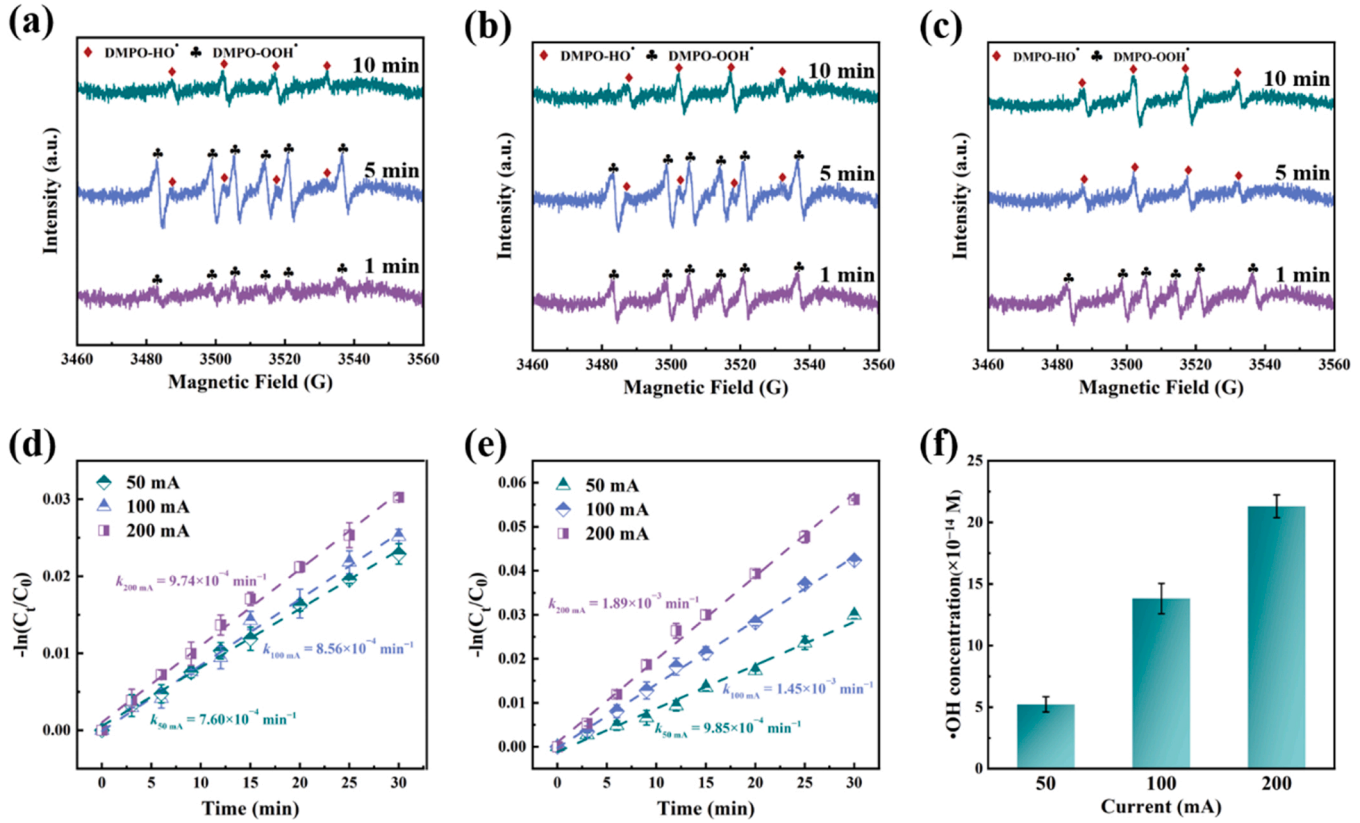

Fig. 4. EPR spectra captured by DMPO for the detection of reactive species in the undivided electrochemical system at a current of (a) 50 mA, (b) 100 mA, and (c) 200 mA. Plots of first-order decay of BA (d) without and (e) with 500 mg L^{-1} Fe(II). (f) Calculated steady-state concentration of •OH. Experimental conditions: initial pH = 3.0, initial Fe(II) concentration = 500 mg L^{-1}, and initial BA concentration = 10 μM.

production of other ROS available in bulk solution, direct anodic oxidation was regarded as the main contributor to the remaining proportion of Fe(II) removal after formate extinction. It is observable from Fig. 5a that the presence of either formate or TBA slightly inhibited Fe(II) oxidation at 50 mA, supporting a prominent role for direct electron transfer in converting Fe(II) to Fe(III). On the contrary, the addition of formate or TBA had a pronounced effect on impeding Fe(II) removal at 100 and 200 mA (Figs. 5b and 5c). The more severe inhibition by formate reflects that the indirect oxidation process via ROS (i.e., •OH) exerts a crucial role in facilitating Fe(II) conversion. The lesser extent of TBA quenching is expected, based on the fact that the production of bulk •OH originated from Fe(II) oxidation via the Haber-Weiss reaction. Moreover, careful comparisons of the data in Fig. 5 indicate that direct oxidation contributed to Fe(II) removal, but the degree of its contribution was highly sensitive to the applied current, although variances between higher currents made little difference. These results, in combination with the data from EPR tests and BA-probe experiments, collectively demonstrate that •OH-induced indirect oxidation occurring far away from the anode surface plays a predominant role in boosting Fe(II) conversion to Fe(III) at high currents.

3.4. *Interpretations of the resulting schwertmannite with lower particle size and higher abundance of –OH groups*

The schwertmannite formed at higher currents with lower particle size and more –OH groups is interpreted with respect to two important

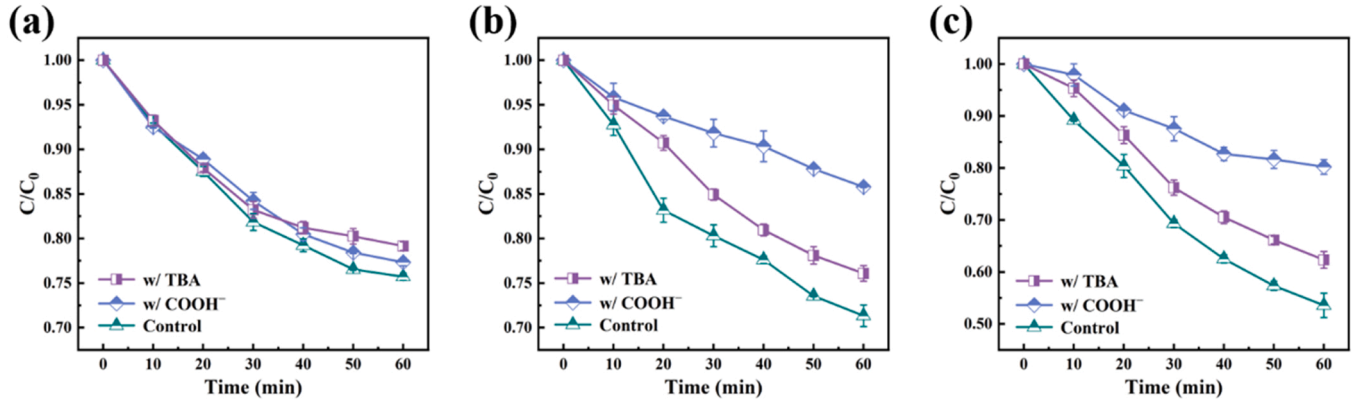

Fig. 5. Effects of scavengers on Fe(II) oxidation in the undivided electrochemical system at a current of (a) 50 mA, (b) 100 mA, and (c) 200 mA. Experimental conditions: initial pH = 3.0, initial Fe(II) concentration = 500 mg L^{-1}, and initial scavenger concentration = 10 mM.

driving forces: ROS-mediated Fe(II) oxidation and increased alkalinity in the vicinity of the cathode. Previous studies have shown that the nucleation and growth mechanism governs the formation of iron(III) (hydr)oxides as a consequence of Fe(II) oxidation [6,16,37], in which the competition between nucleation and growth processes determine the size of oxide particles. At a low current (e.g., 50 mA), Fe(II) oxidation mainly happens surrounding the interface of the anode; as such, the amount of nuclei is limited and the prolonged reaction time causes their continuous growth, leading to the formation of larger particles. By contrast, at a high current (e.g., 200 mA), the •OH-induced Fe(II) oxidation mostly occurs in the bulk solution, which creates more numerous nuclei, thus making the aggregated particles smaller and SSA larger. Given the fact that –OH groups are engaged in the formation of schwertmannite, the cathodically generated alkaline is critical in accelerating its production with higher –OH content. Despite the decrease in bulk pH values from 3.0 to 2.4 in all cases, the localized pH in the vicinity of the cathode increased with current (Fig. S9), owing to more vulnerable OH^- generation from water electrolysis. This dramatically increased cathode pH promotes Fe(II) conversion to schwertmannite containing elevated amounts of –OH. To verify this, a reference experiment was conducted with the divided cell with a BPM, which has the merit of continuously supplementing OH^- to the anode side (Fig. S10a), due to the heterolytic water dissociation in the membrane interface under a reverse bias condition [19,34]. Fig. S10b shows that this scenario exhibited good Fe(II) removal performance, comparable to the undivided system. Also, the resulting schwertmannite had a higher proportion of –OH groups, in accordance with the stoichiometric formulas obtained from the undivided reactor at 200 mA.

To summarize, Fig. 6 illustrates the Fe(II) oxidation pathways in the coupled anodic-cathodic system, which differ depending on the extent of applied current and accordingly control the size and composition of the resulting schwertmannite. Direct Fe(II) oxidation by the anode predominates at lower currents, and proceeds at a lower rate, resulting in the formation of schwertmannite with larger particle size, smaller SSA, and decreased amounts of –OH groups. On the other hand, the higher current induces excessive formation of O_2 (at the anode), which is dissolved in solution and activated by Fe(II) to initiate a series of reactions that generate $•O_2^-$, H_2O_2, and •OH. The availability of higher levels of bulk •OH, in turn, enables the acceleration of Fe(II) oxidation to Fe(III). The involvement of bulk •OH in oxidizing Fe(II) and the burst of OH^- generation (at the cathode) under a higher current are the keys to the formation of schwertmannite with smaller size, larger SSA, and more –OH groups.

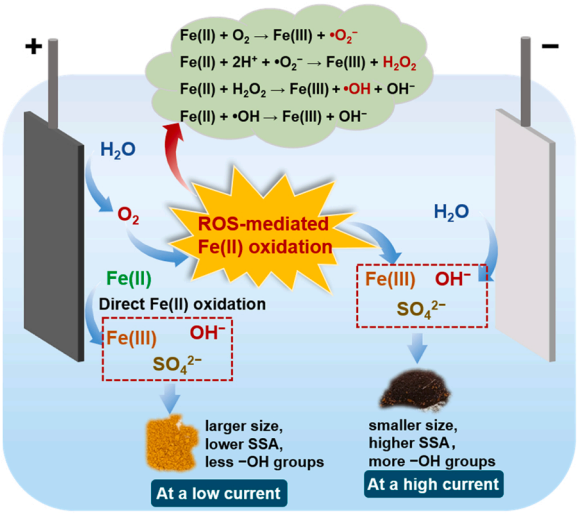

Fig. 6. Proposed mechanisms of Fe(II) oxidation and schwertmannite formation in the coupled anodic-cathodic process: effect of the applied current.

3.5. Recovery of schwertmannite from real AMD using the coupled anodic-cathodic system and its application for As(III)/As(V) adsorption

Toward practical application of these electrochemical methods to environmentally-friendly treatment of AMD, further efforts were made to verify the effectiveness of the coupled anodic-cathodic system for the recovery of schwertmannite from real AMD. Fig. 7a shows a schematic diagram of the electrochemical processes adopted for AMD treatment. Prior to schwertmannite formation, a pretreatment electrolysis step was employed with the purposes of separating/recovering Cu(II) from the aqueous phase and enabling reduction of Fe(III) available in the AMD sample to Fe(II). It should be noted that the single anodic-cathodic process without the involvement of this pretreatment step did not cause successful precipitation of schwertmannite, because the cathodic Cu reduction severely inhibited cathodic alkaline production from water electrolysis. The 3-h batch operation caused nearly complete removal of the Cu(II) and Fe(III) that had been subjected to cathodic reduction. Fig. S11 shows the coverage of high-purity Cu on the cathode, suggesting a promising approach for Cu recovery from AMD. Upon this processing, the concentration of Fe(II) significantly increased from 24.3 to 223.1 mg L^{-1}, again confirming the necessity of the pretreatment step. Afterwards, the coupled anodic-cathodic system enabled formation of precipitates having typical schwertmannite features, as shown in the XRD patterns (Fig. S12). Similar to the operation on the simulated AMD, the higher current for treating real AMD was preferred because of smaller particle size (Fig. S13). It is apparent that Al and Si were included in the solid in addition to Fe, S, and O (Fig. S14); their incorporation into schwertmannite was likely caused by the substitution of Fe by Al [18,38] and the formation of complexes and polymers by silicic acid at the surface [12,14,17].

The conversion percentage of Fe(II) to schwertmannite for one-time operation at 200 mA was 24.76 %, suggesting a considerable number of Fe(III) remained in the solution. The relatively low conversion efficiency was also reported in previous studies [21,31] and can be explained by the insufficient supply of OH^- that was chemically bonded with Fe(III) (this species was rapidly electrogenerated in a large quantity). The multi-cycle operation of the treated AMD via the sequent Fe(III) reduction-Fe(II) oxidation steps (illustrated in Fig. 7a) can substantially enhance the proportion of Fe(II) converted to Fe(III) solid. Table S5 lists that the total Fe(II) recovery efficiency increased with the increasing cycle number and reached 90.29 % upon 4-cycle operation. Also, it is revealed that the stainless steel cathode can withstand the high-acid condition due to the cathodic protection and the system exhibited long-term stability, as the TFe recovery efficiency did not deteriorate after 10 consecutive experiments (Fig. S15). The recovery of schwertmannite from real AMD using the coupled anodic-cathodic system was also demonstrated under the continuous-flow mode, as illustrated in Table S6. It is noticeable that the treatment capacity increased with the decreasing flow rate, with higher extents of Cu, Fe, and SO_4^{2-} removal at a flow rate of 1 mL min^{-1} as compared to 5 mL min^{-1}.

Schwertmannite has a high capacity for adsorption to As(III)/As(V), owing to the exchange of arsenic species with the surface groups of ≡Fe–OH/OH_2 available in schwertmannite [58]. To confirm that the electrochemistry-produced schwertmannite is a sorbent for As(III)/As(V) and that the adsorption capacity is highly sensitive to the intrinsic structure of schwertmannite, comparisons of As(III)/As(V) sorption kinetics and isotherms were conducted between the schwertmannite samples synthesized with the chemical method (H_2O_2 addition) and the electrochemical methods at different currents. The results of kinetic experiments in Fig. S16 show that the adsorption of As(III) and As(V) on all the schwertmannite samples followed a similar pattern: a very steep rise within 120 min, a slow increase up to 240 min, and reaching a relatively stable level from 240 to 360 min. These profiles fit well with a pseudo-second-order kinetic model, implying that the fixation of arsenic species by schwertmannite was by chemisorption [1,46]. However, there was much variation in the equilibrium amount of As(III)/As(V)

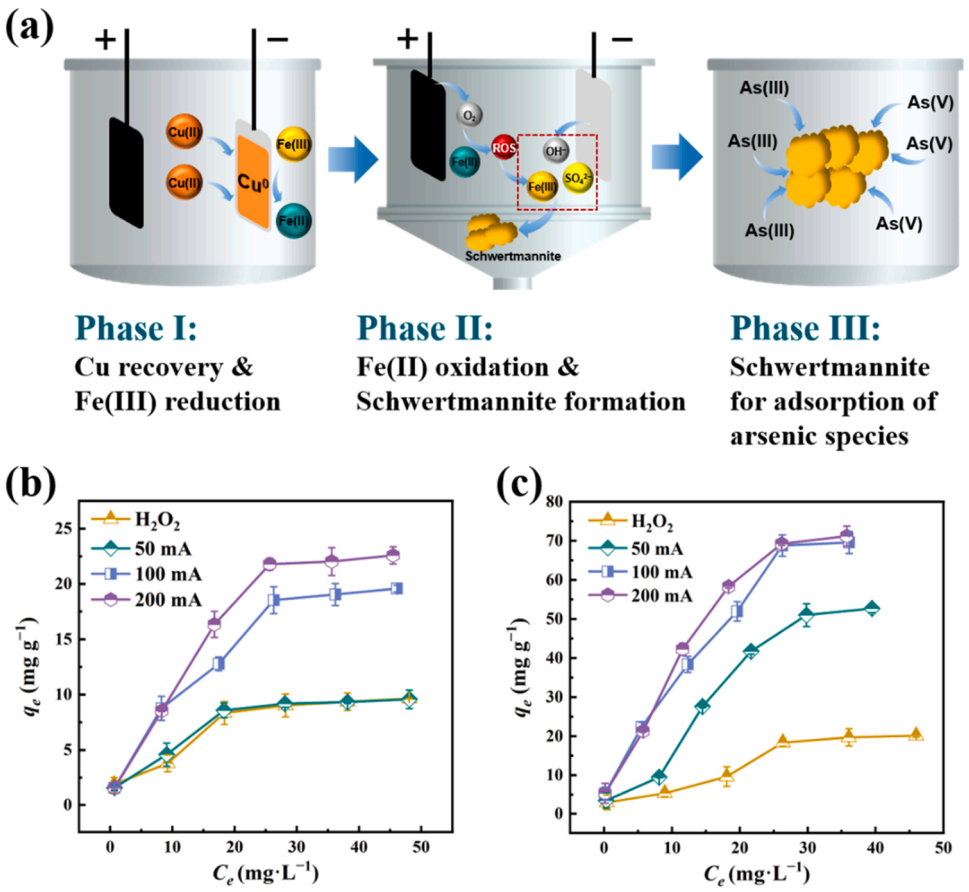

Fig. 7. (a) Schematic diagram of the electrochemical processes adopted for sustainable AMD treatment and resource recovery. Adsorption behaviors of (b) As(III) and (c) As(V) on electrochemistry-resulted schwertmannite synthesized from real AMD. Experimental conditions: 2 mA for Phase I, 200 mA for Phase II, initial arsenic concentration (C_e) varied from 1 to 50 mg L^{-1}, and sorbent (i.e., schwertmannite) dose = 10 mg. q_e is the amount of arsenic species adsorbed per weight of sorbent.

uptake. As expected, the schwertmannite obtained at high currents significantly increased the adsorption of As(III)/As(V) because of larger SSA and elevated contents of –OH groups. Moreover, adsorption of As(V) was faster and had more capacity than for As(III). Such a difference can be explained in terms of the different acidic properties; arsenic acid is a stronger acid than arsenous acid, which thereby favors removal of As(V) by anion-exchange [36].

The equilibrium adsorption isotherms shown in Figs. 7b and 7c can be useful in predicting the adsorption capacity of electrosynthesized schwertmannite. The adsorption of As(III)/As(V) onto all of the investigated materials was precisely simulated with the Langmuir isotherm model (Table S7), suggesting the mechanism of monolayer adsorption [1,46,58]. It is noticeable that the electrogenerated schwertmannite outperformed the chemically synthesized schwertmannite in terms of remarkably enhanced As(III)/As(V) adsorption. For instance, the maximum adsorption capacity of arsenic species was attained with the 200 mA-induced schwertmannite, with a value of 23.81 and 92.80 mg g^{-1} in relation to As(III) and As(V), respectively. On the other hand, these values associated with H_2O_2-induced schwertmannite distinctly declined to 9.75 mg g^{-1} for As(III) and 21.22 mg g^{-1} for As (V). It should be also emphasized that 23.81 mg g^{-1} obtained at pH 3 was higher than the reported values corresponding to whether the schwertmannite was biologically or chemically prepared [4,43,63]. These findings imply that the electrochemical strategy for in situ schwertmannite production is more advantageous to the traditional H_2O_2-induced chemical method, including the avoidance of using external oxidants and the extraordinary adsorption capability of the resultant materials.

4. Conclusions

This study presented a straightforward and convenient electrochemical method of coupling anodically-formed ROS with cathodically generated alkaline to facilitate Fe(II) oxidation and thus promote recovery of schwertmannite from AMD. This method offers some benefits over the conventional chemical method because it was capable of synthesizing schwertmannite with high SSA and abundant –OH groups, desirable properties that make it a promising sorbent. The mechanistic studies showed that the morphological characteristics and chemical structure of schwertmannite were highly dependent on the amount of in-situ generated ROS (i.e., •OH) available in the bulk solution, which is closely linked with the extent of current applied to the circuit. For example, at a low current, Fe(II) oxidation mainly occurs surrounding the anode surface and proceeds at a low rate. The unreacted Fe(II) ions can thus accumulate on the nuclei before they undergo oxidation and aggregation processes to form large particles. At a high current, continuous generation of O_2 is achieved, which is further dissolved in the solution and reacts with Fe(II) to produce a series of ROS. Thus, most Fe(II) ions are consumed during the nucleation process, resulting in smaller size and greater SSA in the eventual particles. In addition, the increasing current caused an increase in the localized pH in the vicinity of the cathode, which prompted the formation of schwertmannite with the involvement of more –OH groups. Importantly, tests with real AMD demonstrated the effectiveness of the coupled anodic-cathodic system for synthesis of schwertmannite that is a promising sorbent for removal of As(III)/As(V) from the aqueous phase.

Environmental Implications

Sustainable acid mine drainage (AMD) treatment with resource recovery has attracted increasing attention in recent years. Herein, we demonstrate that a coupled electrochemical system involving anodically-formed reactive oxygen species with cathodically generated alkaline facilitates in situ synthesis of schwertmannite from AMD. We discover that the •OH-mediated pathway rather than the direct oxidation pathway, plays a dominant role in accelerating Fe(II) oxidation especially at high currents, which is beneficial to the formation of schwertmannite high in SSA and amounts of –OH groups. Importantly, we show that schwertmannite electrosynthesized from real AMD functions as a powerful sorbent in removal of arsenic species.

CRediT authorship contribution statement

Ziyuan Huang: Methodology, Investigation, Formal analysis, Data curation, Visualization, Writing – original draft. **Huanxin Ma:** Methodology, Investigation. **Chengshuai Liu:** Resources, Supervision. **Fangyuan Meng:** Resources, Validation. **Jyh-Fu Lee:** Resources, Validation. **Yu-Jung Lin:** Resources, Validation. **Xiaoyun Yi:** Supervision. **Zhi Dang:** Supervision, Project administration. **Chunhua Feng:** Conceptualization, Writing – review & editing, Supervision, Project administration, Funding acquisition.

Declaration of Competing Interest

The authors declare that they have no known competing financial interests or personal relationships that could have appeared to influence the work reported in this paper.

Data Availability

Data will be made available on request.

Acknowledgements

We gratefully acknowledge financial support from the National Natural Science Foundation of China (Nos. U21A2034 and 21876052); the Guangdong Special Support Plan for Innovation Teams (No. 2019BT02L218); the Guangdong Special Support Plan for Young Top-notch Talents (No. 2019TQ05L179); the Science and Technology Planning Project of Guangdong Province, China (No. 2019A050510009); and the Natural Science Foundation of Guangdong Province, China (No. 2021B1515120077).

Appendix A. Supporting information

Supplementary data associated with this article can be found in the online version at doi:10.1016/j.jhazmat.2023.131075.

References

[1] Antelo, J., Fiol, S., Gondar, D., López, R., Arce, F., 2012. Comparison of arsenate, chromate and molybdate binding on schwertmannite: surface adsorption vs anion-exchange. J Colloid Interface Sci 386 (1), 338–343.
[2] Blgham, J.M., Schwertmann, U., Carlson, L., Murad, E., 1990. A poorly crystallized oxyhydroxysulfate of iron formed by bacterial oxidation of Fe(II) in acid mine waters. Geochim Cosmochim Acta 54 (10), 2743–2758.
[3] Boily, J.-F., Gassman, P.L., Peretyazhko, T., Szanyi, J., Zachara, J.M., 2010. FTIR spectral components of schwertmannite. Environ Sci Technol 44 (4), 1185–1190.
[4] Burton, E.D., Bush, R.T., Johnston, S.G., Watling, K.M., Hocking, R.K., Sullivan, L. A., et al., 2009. Sorption of arsenic(V) and arsenic(III) to schwertmannite. Environ Sci Technol 43 (24), 9202–9207.
[5] Burton, E.D., Johnston, S.G., Kraal, P., Bush, R.T., Claff, S., 2013. Sulfate availability drives divergent evolution of arsenic speciation during microbially mediated reductive transformation of schwertmannite. Environ Sci Technol 47 (5), 2221–2229.
[6] Chen, M., Wu, J., Sun, J., Li, C., Mai, X., Lu, G., et al., 2021. Mechanism and formation process of schwertmannite under electrochemical deposition. Colloids Surf A Physicochem Eng Asp 617, 126366.
[7] Chen, Y.-t., Li, J.-t., Chen, L.-x., Hua, Z.-s., Huang, L.-n., Liu, J., et al., 2014. Biogeochemical processes governing natural pyrite oxidation and release of acid metalliferous drainage. Environ Sci Technol 48 (10), 5537–5545.
[8] Chen, Y., Yu, G., Chen, W., Liu, Y., Li, G.-D., Zhu, P., et al., 2017. Highly active, nonprecious electrocatalyst comprising borophene subunits for the hydrogen evolution reaction. J Am Chem Soc 139 (36), 12370–12373.
[9] Cho, K., Hoffmann, M.R., 2015. $Bi_xTi_{1-x}O_z$ functionalized heterojunction anode with an enhanced reactive chlorine generation efficiency in dilute aqueous solutions. Chem Mater 27 (6), 2224–2233.
[10] Cifuentes, L., Glasner, R., 2003. Kinetics of the electrolytic Fe^{2+}/Fe^{3+} oxidation on various anode materials. Rev Metal 260–267.
[11] Collins, R.N., Rosso, K.M., Rose, A.L., Glover, C.J., David Waite, T., 2016. An in situ XAS study of ferric iron hydrolysis and precipitation in the presence of perchlorate, nitrate, chloride and sulfate. Geochim Cosmochim Acta 177, 150–169.
[12] Doelsch, E., Stone, W.E.E., Petit, S., Masion, A., Rose, J., Bottero, J.-Y., et al., 2001. Speciation and crystal chemistry of Fe(III) chloride hydrolyzed in the presence of SiO_4 Ligands. 2. Characterization of Si−Fe aggregates by FTIR and 29Si solid-state NMR. Langmuir 17 (5), 1399–1405.
[13] Dold, B., 2008. Sustainability in metal mining: from exploration, over processing to mine waste management. Rev Environ Sci Bio/Technol 7 (4), 275–285.
[14] Eick, M.J., Luxton, T.P., Welsh, H.A., 2009. Effect of silica polymerization on the oxalate-promoted dissolution of goethite. Clays Clay Min 57 (5), 578–585.
[15] Feng, K., Wang, X., Ding, B., Xu, M., Liang, J., Zhou, L., 2022. Acidithiobacillus ferrooxidans mediates morphology evolution of schwertmannite in the presence of Fe^{2+}. Chem Geol 598, 120828.
[16] Feng, K., Wang, X., Zhou, B., Xu, M., Liang, J., Zhou, L., 2021. Hydroxyl, Fe^{2+}, and Acidithiobacillus ferrooxidans jointly determined the crystal growth and morphology of schwertmannite in a sulfate-rich acidic environment. ACS Omega 6 (4), 3194–3201.
[17] French, R.A., Caraballo, M.A., Kim, B., Rimstidt, J.D., Murayama, M., Hochella, M. F., 2012. The enigmatic iron oxyhydroxysulfate nanomineral schwertmannite: morphology, structure, and composition. Am Mineral 97 (8–9), 1469–1482.
[18] Gan, M., Zheng, Z., Sun, S., Zhu, J., Liu, X., 2015. The influence of aluminum chloride on biosynthetic schwertmannite and Cu(II)/Cr(VI) adsorption. RSC Adv 5 (114), 94500–94512.
[19] Giesbrecht, P.K., Freund, M.S., 2020. Recent advances in bipolar membrane design and applications. Chem Mater 32 (19), 8060–8090.
[20] Haber, F., Weiss, J., 1932. Über die katalyse des hydroperoxydes. Sci Nat -Heide 20 (51), 948–950.
[21] Huang, S., Zhou, L., 2012. Fe^{2+} oxidation rate drastically affect the formation and phase of secondary iron hydroxysulfate mineral occurred in acid mine drainage. Mater Sci Eng C 32 (4), 916–921.
[22] Jin, X., Guo, C., Li, X., Liao, Y., Yao, Q., Lu, G., et al., 2021. Arsenic partitioning during schwertmannite dissolution and recrystallization in the presence of Fe(II) and oxalic acid. ACS Earth Space Chem 5 (5), 1058–1070.
[23] Jones, A.M., Griffin, P.J., Collins, R.N., Waite, T.D., 2014. Ferrous iron oxidation under acidic conditions – the effect of ferric oxide surfaces. Geochim Cosmochim Acta 145, 1–12.
[24] Kanzaki, Y., Murakami, T., 2013. Rate law of Fe(II) oxidation under low O_2 conditions. Geochim Cosmochim Acta 123, 338–350.
[25] Koppenol, W.H., 2001. The Haber-Weiss cycle – 70 years later. Redox Rep 6 (4), 229–234.
[26] Lei, Y., Song, B., van der Weijden, R.D., Saakes, M., Buisman, C.J.N., 2017. Electrochemical induced calcium phosphate precipitation: importance of local pH. Environ Sci Technol 51 (19), 11156–11164.
[27] Lei, Z., Huang, Z., Lin, Y., Liu, Y., Yan, Z., Zheng, W., et al., 2022.) Boosting the oxidative capacity of the Fe(0)/O_2 system via an air-breathing cathode. J Hazard Mater 438, 129552.
[28] Li, X., Liu, L., Wu, Y., Liu, T., 2019. Determination of the redox potentials of solution and solid surface of Fe(II) associated with iron oxyhydroxides. ACS Earth Space Chem 3 (5), 711–717.
[29] Liao, Y., Zhou, L., Liang, J., Xiong, H., 2009. Biosynthesis of schwertmannite by Acidithiobacillus ferrooxidans cell suspensions under different pH condition. Mater Sci Eng C 29 (1), 211–215.
[30] Ling, C., Wu, S., Han, J., Dong, T., Zhu, C., Li, X., et al., 2022. Sulfide-modified zero-valent iron activated periodate for sulfadiazine removal: performance and dominant routine of reactive species production. Water Res 220, 118676.
[31] Liu, F.W., Zhou, J., Zhang, S.S., Liu, L.L., Zhou, L.X., Fan, W.H., 2015. Schwertmannite synthesis through ferrous ion chemical oxidation under different H_2O_2 supply rates and its removal efficiency for arsenic from contaminated groundwater. PLoS One 10, 9.
[32] Liu, L., Guo, D., Qiu, G., Liu, C., Ning, Z., 2022. Photooxidation of Fe(II) to schwertmannite promotes As(III) oxidation and immobilization on pyrite under acidic conditions. J Environ Manag 317, 115425.
[33] Liu, M., Feng, Z., Luan, X., Chu, W., Zhao, H., Zhao, G., 2021. Accelerated Fe^{2+} regeneration in an effective electro-fenton process by boosting internal electron transfer to a nitrogen-conjugated Fe(III) complex. Environ Sci Technol 55 (9), 6042–6051.
[34] Liu, Y., Yan, Z., Chen, R., Yu, Y., Chen, X., Zheng, X., et al., 2019. 2,4-Dichlorophenol removal from water using an electrochemical method improved by a composite molecularly imprinted membrane/bipolar membrane. J Hazard Mater 377, 259–266.

[35] Luo, Y., Tang, L., Khan, U., Yu, Q., Cheng, H.-M., Zou, X., et al., 2019. Morphology and surface chemistry engineering toward pH-universal catalysts for hydrogen evolution at high current density. Nat Commun 10 (1), 269.
[36] Muñoz, J.A., Gonzalo, A., Valiente, M., 2002. Arsenic adsorption by Fe(III)-loaded open-celled cellulose sponge. Thermodynamic and selectivity aspects. Environ Sci Technol 36 (15), 3405–3411.
[37] Neil, C.W., Lee, B., Jun, Y.-S., 2014. Different arsenate and phosphate incorporation effects on the nucleation and growth of iron(III) (Hydr)oxides on quartz. Environ Sci Technol 48 (20), 11883–11891.
[38] Paikaray, S., Essilfie-Dughan, J., Hendry, M.J., 2018. Ionic substitution of Mg^{2+} for Al^{3+} and Fe^{3+} with octahedral coordination in hydroxides facilitate precipitation of layered double hydroxides. Geochim Cosmochim Acta 220, 217–234.
[39] Paikaray, S., Göttlicher, J., Peiffer, S., 2011. Removal of As(III) from acidic waters using schwertmannite: surface speciation and effect of synthesis pathway. Chem Geol 283 (3), 134–142.
[40] Paikaray, S., Schröder, C., Peiffer, S., 2017. Schwertmannite stability in anoxic Fe (II)-rich aqueous solution. Geochim Cosmochim Acta 217, 292–305.
[41] Pierre Louis, A.-M., Yu, H., Shumlas, S.L., Van Aken, B., Schoonen, M.A.A., Strongin, D.R., 2015. Effect of phospholipid on pyrite oxidation and microbial communities under simulated acid mine drainage (AMD) conditions. Environ Sci Technol 49 (13), 7701–7708.
[42] Qi, Z., Li, G., Wang, M., Chen, C., Xu, Z., An, T., 2022. Photoelectrocatalytic inactivation mechanism of E. coli DH5α (TET) and synergistic degradation of corresponding antibiotics in water. Water Res 215, 118240.
[43] Qiao, X., Liu, L., Shi, J., Zhou, L., Guo, Y., Ge, Y., et al., 2017. Heating changes bio-Schwertmannite microstructure and arsenic(III) removal efficiency. Minerals 7 (1), 9.
[44] Ravel, B., Newville, M., 2005. ATHENA, ARTEMIS, HEPHAESTUS: data analysis for X-ray absorption spectroscopy using IFEFFIT. J Synchrotron Radiat 12 (4), 537–541.
[45] Regenspurg, S., Brand, A., Peiffer, S., 2004. Formation and stability of schwertmannite in acidic mining lakes. M. Eggleston. Geochim Cosmochim Acta 68 (6), 1185–1197.
[46] Regenspurg, S., Peiffer, S., 2005. Arsenate and chromate incorporation in schwertmannite. Appl Geochem 20 (6), 1226–1239.
[47] Rose, A.L., Waite, T.D., 2002. Kinetic model for Fe(II) oxidation in seawater in the absence and presence of natural organic matter. Environ Sci Technol 36 (3), 433–444.
[48] Rossmeisl, J., Qu, Z.W., Zhu, H., Kroes, G.J., Nørskov, J.K., 2007. Electrolysis of water on oxide surfaces. J Electroanal Chem 607 (1), 83–89.
[49] Sabarathinam, C., Bhandary, H., Al-Khalid, A., 2020. Tracing the evolution of acidic hypersaline coastal groundwater in Kuwait. Arab J Geosci 13 (21), 1146.
[50] Santana-González, C., Santana-Casiano, J.M., González-Dávila, M., Santana-del Pino, A., Gladyshev, S., Sokov, A., 2018. Fe(II) oxidation kinetics in the North Atlantic along the 59.5° N during 2016. Mar Chem 203, 64–77.
[51] Shu, Z., Liu, L., Qiu, G., Yang, X., Zhang, M., Tan, W., et al., 2019. Photochemical formation process of schwertmannite on montmorillonite and corresponding Cr (VI) adsorption capacity. ACS Earth Space Chem 3 (5), 718–727.
[52] Singer, P.C., Stumm, W., 1970. Acidic mine drainage: the rate-determining step. Science 167 (3921), 1121–1123.
[53] Song, Y., Guo, Z., Wang, R., Yang, L., Cao, Y., Wang, H., 2022. A novel approach for treating acid mine drainage by forming schwertmannite driven by a combination of biooxidation and electroreduction before lime neutralization. Water Res 221, 118748.
[54] Trasatti, S., 1984. Electrocatalysis in the anodic evolution of oxygen and chlorine. Electrochim Acta 29 (11), 1503–1512.
[55] Wang, S., Pei, S., Zhang, J., Huang, J., You, S., 2022. Flow-through electrochemical removal of benzotriazole by electroactive ceramic membrane. Water Res 218, 118454.
[56] Wang, X., Gu, C., Feng, X., Zhu, M., 2015. Sulfate local coordination environment in schwertmannite. Environ Sci Technol 49 (17), 10440–10448.
[57] Wang, X., Jiang, H., Fang, D., Liang, J., Zhou, L., 2019. A novel approach to rapidly purify acid mine drainage through chemically forming schwertmannite followed by lime neutralization. Water Res 151, 515–522.
[58] Wang, X., Ying, H., Zhao, W., Feng, X., Tan, W., Beyer, K.A., et al., 2021. Molecular-scale understanding of sulfate exchange from schwertmannite by chromate versus arsenate. Environ Sci Technol 55 (9), 5857–5867.
[59] Xiong, H., Liao, Y., Zhou, L., 2008. Influence of chloride and sulfate on formation of akaganéite and schwertmannite through ferrous biooxidation by acidithiobacillus ferrooxidans cells. Environ Sci Technol 42 (23), 8681–8686.
[60] Yamazaki, I., Piette, L.H., 1991. EPR spin-trapping study on the oxidizing species formed in the reaction of the ferrous ion with hydrogen peroxide. J Am Chem Soc 113 (20), 7588–7593.
[61] Yan, Z., Dai, Z., Zheng, W., Lei, Z., Qiu, J., Kuang, W., et al., 2021. Facile ammonium oxidation to nitrogen gas in acid wastewater by in situ photogenerated chlorine radicals. Water Res 205, 117678.
[62] Ying, H., Feng, X., Zhu, M., Lanson, B., Liu, F., Wang, X., 2020. Formation and transformation of schwertmannite through direct Fe^{3+} hydrolysis under various geochemical conditions. Environ Sci-Nano 7 (8), 2385–2398.
[63] Zhang, D., Wu, S., Wei, Y., Zhou, L., 2022. Schwertmannite modified with ethanol: a simple and feasible method for improving As(III) adsorption capacity. J Environ Chem Eng 10 (3), 107412.
[64] Zhang, J., Ji, Q., Lan, H., Zhang, G., Liu, H., Qu, J., 2019. Synchronous reduction–oxidation process for efficient removal of trichloroacetic acid: H* initiates dechlorination and ·OH is responsible for removal efficiency. Environ Sci Technol 53 (24), 14586–14594.
[65] Zhang, Y., Li, S., Fan, S., Wu, Y., Hu, H., Feng, Z., et al., 2021. A stepwise processing strategy for treating highly acidic wastewater and comprehensive utilization of the products derived from different treating steps. Chemosphere 280, 130646.
[66] Zhou, J.-X., Zhou, Y.-J., Zhang, J., Dong, Y., Liu, F.-W., Wu, Z.-H., et al., 2022. Effect of pH regulation on the formation of biogenic schwertmannite driven by Acidithiobacillus ferrooxidans and its arsenic removal ability. Environ Technol 43 (24), 3706–3718.
[67] Zhu, M., Legg, B., Zhang, H., Gilbert, B., Ren, Y., Banfield, J.F., et al., 2012. Early stage formation of iron oxyhydroxides during neutralization of simulated acid mine drainage solutions. Environ Sci Technol 46 (15), 8140–8147.